



Quantum microscopy based on Hong–Ou–Mandel interference

Bienvenu Ndagano¹, Hugo Defienne¹, Dominic Branford², Yash D. Shah¹, Ashley Lyons¹, Niclas Westerberg¹, Erik M. Gauger² and Daniele Faccio¹✉

Hong–Ou–Mandel (HOM) interference—the bunching of indistinguishable photons at a beamsplitter—is a staple of quantum optics and lies at the heart of many quantum sensing approaches and recent optical quantum computers. Here we report a full-field, scan-free quantum imaging technique that exploits HOM interference to reconstruct the surface depth profile of transparent samples. We demonstrate the ability to retrieve images with micrometre-scale depth features with photon flux as small as seven photon pairs per frame. Using a single-photon avalanche diode camera, we measure both bunched and anti-bunched photon-pair distributions at the output of an HOM interferometer, which are combined to provide a lower-noise image of the sample. This approach demonstrates the possibility of HOM microscopy as a tool for the label-free imaging of transparent samples in the very low photon regime.

The bunching of indistinguishable photons at the outputs of a beamsplitter (BS) is the key signature of the Hong–Ou–Mandel (HOM) effect¹. Since its first demonstration, this effect has found many applications in various fields of quantum optics such as quantum state engineering^{2,3}, quantum information processing^{4,5} and quantum metrology^{6,7}. In the context of quantum imaging, HOM interference has been exploited to engineer quantum states through post-selection with spatial light modulators and single-pixel detectors, as well as multiphoton ghost imaging^{8,9}. One of the drawbacks of this approach is that it involves reconstructing the image one spatial mode at a time. To circumvent this limitation, there has been growing interest in single-photon cameras and related imaging opportunities^{10–12} such as the characterization of quantum correlations and entanglement^{13–17}, ghost imaging^{18,19}, quantum holography²⁰, imaging with undetected photons²¹, imaging through noise^{22,23}, N00N-state imaging^{24,25} and entanglement-enabled holography²⁶. It is worth noting that although many of the schemes mentioned above have relied on charge-coupled device (CCD) technology, next-generation single-photon avalanche photodiode (SPAD) cameras with high temporal resolution, high pixel count and high frame rates are poised to enable even more exciting pathways in quantum imaging^{27,28}.

In the context of HOM interferometry, another study demonstrated the measurement of spatial structure of a single photon using an intensified CMOS camera²⁹; spatial indistinguishability between the photons is altered by a digital hologram, leading to varying degrees of photon bunching, revealing the shape of the hologram. It is, however, worth noting that this demonstration evaluated the indistinguishability of two single-mode twin beams that were filtered with single-mode fibres. A similar approach was taken in another study for full-field quantum optical coherence tomography³⁰; by scanning the delay between twin photons, the image of a sample was reconstructed using an intensified CCD camera. Although multimode HOM sensing has been shown elsewhere³¹ where they replaced single-pixel detectors with two electron-multiplying CCD cameras for coincidence counting, there are no reports on a multimode HOM imaging technique to the best of our knowledge. Such a scheme will have the potential benefit of

higher spatial resolution compared with single-mode illumination. In addition, a wide-field technique would enable bio-imaging without any scanning parts, substantially reducing acquisition times and still operating in the very low photon regime.

Rather than competing with classical imaging techniques, quantum imaging offers complementary benefits and provides additional opportunities such as low-light imaging or more robust interferometric sensing approaches. The former may be crucial for delicate photoactive samples, whereas the latter derives from measuring interference via photon correlations, making it robust to perturbations that extinguish classical interferometric fringes.

Here we demonstrate a full-field, scan-free, quantum imaging technique enabled by HOM interference. The scheme exploits the fact that group-velocity delays along the rising (or falling) edge of the HOM interference signal have a 1:1 mapping to the coincidence rate. We spatially resolve the HOM interference across multiple spatial modes by reconstructing the two-photon spatial joint probability distribution (JPD) at every pixel position of an SPAD camera, from which we extract both photon-bunching and photon-anti-bunching information. We can choose to use the latter to obtain the depth profile of samples such as a pattern of clear acrylic sprayed over a microscope slide with an average depth of $\sim 13\ \mu\text{m}$ or a pattern etched on a glass substrate of $\sim 8\ \mu\text{m}$ depth. In both cases, we observe that the depth profile of the sample is not accessible through a direct intensity measurement. However, when observed with the HOM imaging system, we obtain a contrast image that does reveal the structure of the object. Image resolution is enhanced via a standard 2×2 camera raster-scanning technique, whereas noise in the image is reduced by combining information from both bunched and anti-bunched photons and based on ideas recently introduced elsewhere⁷. The combination of these approaches and the high frame rates of the SPAD camera allow the efficient imaging of micrometre-sized features at very low photon levels.

Concept

The idea behind our HOM imaging technique is shown in Fig. 1. The paths of two indistinguishable photons are overlapped onto a

¹School of Physics and Astronomy, University of Glasgow, Glasgow, UK. ²SUPA, Institute of Photonics and Quantum Sciences, Heriot-Watt University, Edinburgh, UK. ✉e-mail: Daniele.Faccio@glasgow.ac.uk

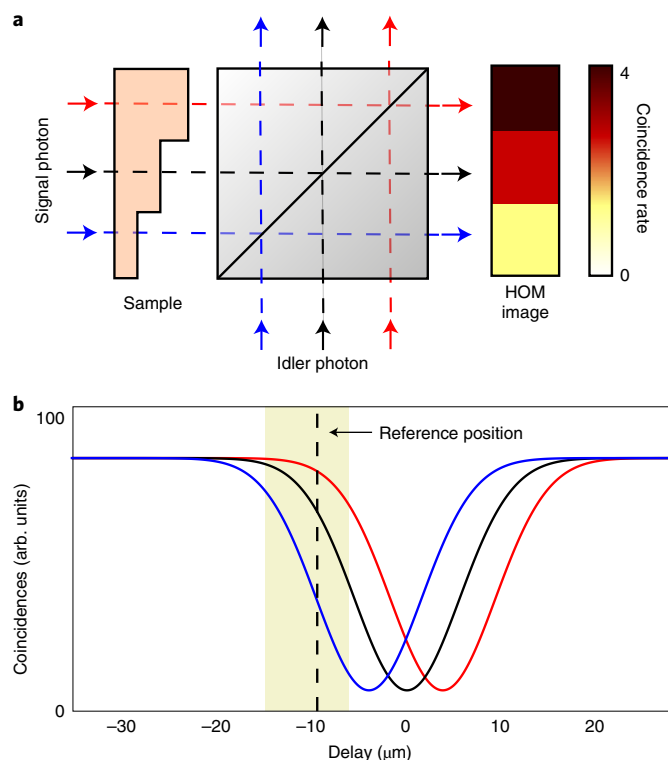


Fig. 1 | Principles of HOM imaging. **a**, In the HOM interferometer, the paths of two indistinguishable photons, namely, signal and idler, overlap on a 50/50 BS. The signal photon traverses a transparent sample of varying thicknesses, and the outputs of the BS are, according to colour, measured in coincidences. **b**, When adjusting the idler delay to the reference position (dashed line), the three paths map different coincidence probabilities, allowing one to obtain a contrast image of the transparent sample for a range of depths indicated by the shaded area. This can be used to reconstruct the depth-thickness variation across the sample.

50/50 BS. A (signal) photon travels through a sample with varying thicknesses, whereas the other (idler) photon does not. For each of the three colour-coded trajectories, the signal photon incurs different group-velocity delays, leading to different arrival times with respect to the idler photon on the matching trajectory. Coincidence measurements on each of the colour-coded paths at the outputs of the BS show that the two-photon interference signals are shifted with respect to each other. By recording the coincidence rates in each of the colour-coded paths, one can obtain a contrast image of the sample. Figure 1b illustrates the mapping between spatial delay and coincidence probability when measuring at a fixed-delay reference position, which can be exploited to reconstruct the relative depth profile of the sample from its HOM image without any need for scanning the HOM interferometer delay.

Compared with classical interferometric or phase-imaging approaches, HOM interference does not require phase stability of the setup, yet it can achieve similar depth-resolution sensitivity of 1–10 nm (ref. 6). The simple approach described here that operates at a fixed delay position at the HOM dip edge (rather than scanning the interferometer across the dip) can achieve an axial (depth) resolution of 100 nm even on a mobile platform³². Different from classical interferometry, the ‘axial field of view’ (distance over which the sample depth can be resolved) can be substantially larger than the optical wavelength and is determined by the half-width of the HOM dip (which, in turn, is fixed by the spontaneous parametric downconversion (SPDC) spectral bandwidth). This is of the order of $\sim 20 \mu\text{m}$ in our experiments.

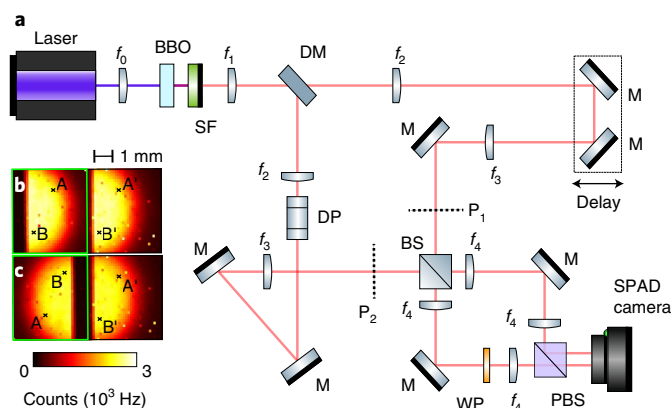


Fig. 2 | HOM imaging setup. **a**, A 0.7-mm-diameter (measured at $1/e^2$ of the intensity maximum) collimated pump beam from a 347 nm pulsed laser with a 100 MHz repetition rate is focused into a 0.5-mm-long BBO crystal where photons pairs are generated through a type-I SPDC. Signal and idler photons are separated in the far field of the BBO crystal using a D-shaped mirror (DM). The signal photon is sent through a delay line where the optical path can be adjusted using a motorized stage with a $1 \mu\text{m}$ step size. The idler photon propagates through a dove prism (DP) that performs an inversion around the x axis. The plane of the DM is relayed to planes P_1 and P_2 using two identical $4f$ imaging systems with $\times 2$ magnification. Subsequently, planes P_1 and P_2 are overlapped and imaged onto the SPAD camera using two identical $4f$ telescopes with $\times 1$ magnification. **b**, Intensity image acquired by the SPAD camera, where spatial positions A (B) and A' (B') map to photon paths from the two output ports of the BS. **c**, We apply a π rotation to one-half of the image (enclosed in the green box) such that the measured signal and idler photons A (B) and A' (B'), respectively, are spatially anti-correlated. $f_0 = 300 \text{ mm}$; $f_1 = 100 \text{ mm}$; $f_2 = 100 \text{ mm}$; $f_3 = 200 \text{ mm}$; $f_4 = 150 \text{ mm}$; SF, spectral filter; BS, 50:50 beamsplitter; PBS, polarization beamsplitter; WP, half-wave plate; M, mirror.

Experimental setup. The layout of the HOM imaging system is depicted in Fig. 2a (Methods). Signal–idler photon pairs are generated via SPDC and are spatially separated in the far field using a D-shaped mirror. The signal and idler photons propagate through identical $4f$ imaging systems that relay the far field to planes P_1 and P_2 —the sample to be imaged is placed in P_2 . The image of planes P_1 and P_2 are overlapped using a 50:50 BS and imaged, using identical imaging systems, onto an SPAD camera (SPC³, MPD) with an array of 32×64 pixels, 80% fill factor and $150 \mu\text{m}$ pixel pitch that can acquire up to 96,000 frames per second.

The two outputs from the BS are shown in Fig. 2b, where pixel positions A (B) and A' (B') map to photon paths in the two outputs of the BS. In the event of bunching, pairs of photons would be detected at either A (B) or A' (B'). Meanwhile, in the event of anti-bunching, one photon in a pair would be detected at A (B) and the other at A' (B'). By applying π rotation on one of the output arms, we note that spatially correlated pair detection indicates bunching, whereas spatially anti-correlated pair detection indicates anti-bunching.

HOM sensing. At the plane of the SPAD camera, we reconstructed the signal (s) and idler (i) JPD, $\Gamma(\mathbf{r}_s, \mathbf{r}_i)$, using the following model³³:

$$\Gamma(\mathbf{r}_s, \mathbf{r}_i) = \frac{1}{N} \sum_{l=1}^N I_l(\mathbf{r}_s) I_l(\mathbf{r}_i) - \frac{1}{N^2} \sum_{m,n=1}^N I_m(\mathbf{r}_s) I_n(\mathbf{r}_i), \quad (1)$$

where $I_l(\mathbf{r}) \in \{0, 1\}$ is the binary value returned by the SPAD sensor for a pixel at location \mathbf{r} in the l th frame. Over the acquisition time of the camera (set here to $10 \mu\text{s}$), the sensor may measure

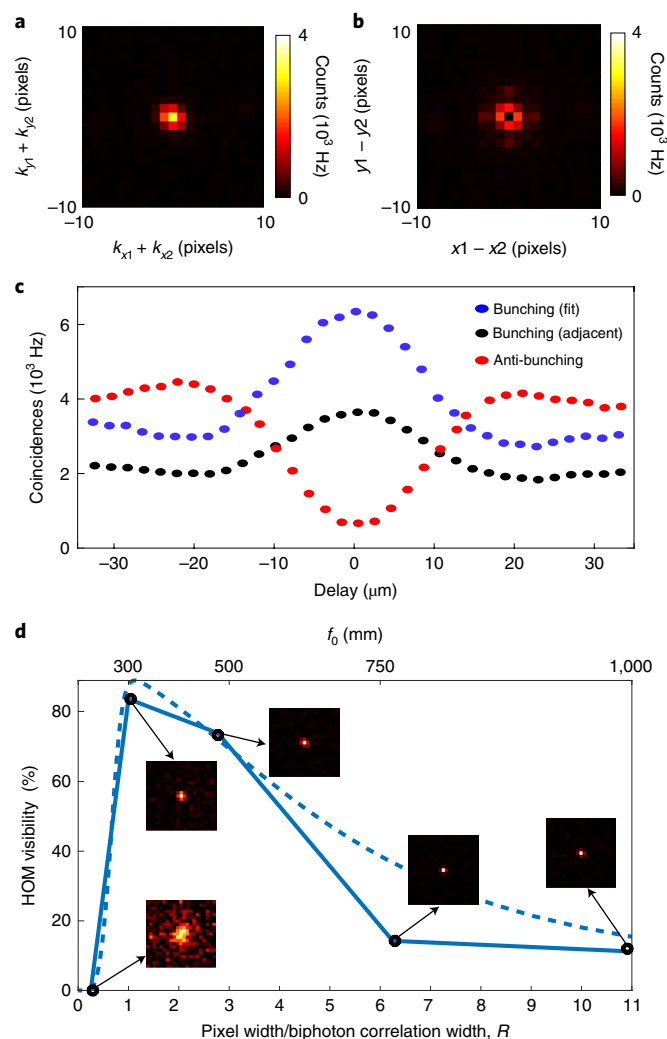


Fig. 3 | HOM sensing with an SPAD camera. **a**, Following the reconstruction of the two-photon spatial distribution and its projection onto the sum coordinates, a correlation peak is revealed corresponding to the number of photons measured at anti-correlated positions (anti-bunching). **b**, Similarly, the projection onto the minus coordinates evaluates the number of bunched photons. The fraction of bunched photons can be evaluated by either fitting a peak or measuring the signal from adjacent pixels. **c**, By scanning the delay stage, we measure the HOM interference. The legend indicates the anti-bunching results (HOM interference dip) and bunching results (HOM interference peak) under the two approximations tested (error bars indicate standard error of the mean and they are the same size or smaller than the dots). At each delay position, we acquire and analyse, on average, 19 million intensity frames. **d**, HOM interference visibility versus focal length of the focusing lens of the parametric downconversion pump (top axis) and ratio R of the camera pixel width to the biphoton correlation width (bottom axis). The highest visibility is observed when the pump is focused such that the two-photon correlation width is equal to the camera pixel pitch. The insets show the normalized sum-coordinate projections of the JPD for different pump-lens focal lengths (plotted over 10×10 pixels). The dashed curve is a parameter-free model used to calculate the HOM dip visibility for our experiment.

photons from multiple pairs. The intra-frame correlation in equation (1) (first term on the right-hand side) estimates the number of coincidences from photons belonging to the same pair (genuine coincidences), as well as those from different pairs (accidental

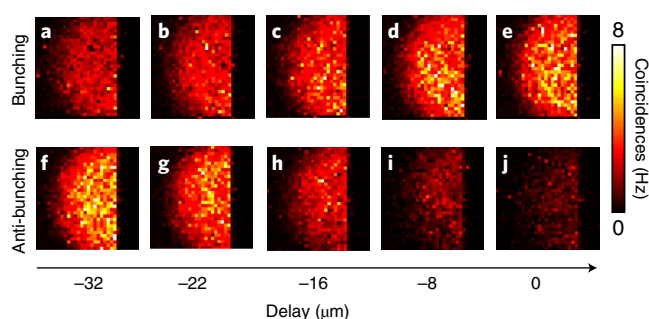


Fig. 4 | Full-field HOM sensing. **a–j**, Spatial images (32×32 pixels) of photon coincidences arising from bunching (**a–e**) and anti-bunching (**f–j**), reconstructed as a function of spatial delay between the signal and idler photons. The bunching images are obtained by measuring coincidences across adjacent pixels. At each delay position, the two-photon distribution is reconstructed from an average of 19 million intensity frames. The pixel pitch is $150 \mu\text{m}$.

coincidences). The latter are estimated and removed from the reconstructed JPD by subtracting the inter-frame correlations (second term on the right-hand side).

As highlighted above in the experimental configuration, anti-bunching events are registered as pair detections from spatially anti-correlated photons and are estimated by projecting the JPD onto the sum coordinates (Fig. 3a). The height of the measured correlation peak indicates the number of reconstructed anti-bunching events. The number of bunching events can be extracted from the pair detections of spatially correlated photons, that is, we project the JPD onto the minus coordinates (Fig. 3b). In this case, we do not have a correlation peak because the pixels on the SPAD camera are not able to ‘photon-number-resolve’. Therefore, it is not possible to directly measure the events of two photons incident on the same pixel.

We then characterized the HOM dip (peak) from two-photon interference by scanning the signal-arm delay stage and evaluated the number of anti-bunching and bunching events at each pixel (Fig. 3c); we obtain an HOM dip with a visibility of $88 \pm 2\%$ (red circles). Then, to estimate the number of bunching events, we can either fit a Gaussian peak to estimate the correlation amplitude of the central pixel (Fig. 3c, blue circles; $81 \pm 7\%$ visibility) or simply average over the four nearest neighbours to the central pixel (Fig. 3c, black circles; $60 \pm 7\%$ visibility). As expected, the latter has lower visibility, but it was the preferred option in the following results as it only relies on the measured data (Methods).

Tailoring the two-photon correlation. The spatial width of two-photon correlation provides a measurement of the average mode width and plays a key role in optimizing the HOM visibility measured by the camera. The correlation width can be controlled by the pump diameter as this determines the number of modes and divergence (k -vector spectrum) of the SPDC. Figure 3d shows the measured HOM dip visibility as we vary the pump-beam diameter on the SPDC crystal by changing the pump-beam focusing lens, f_0 (upper horizontal axis), or equivalently, as a function of the ratio R of the pixel width to the biphoton correlation width (lower horizontal axis; Methods). If the correlation width is much smaller than the camera pixel pitch (large focal lengths and loose pump focusing), then many modes overlap at the same pixel. If the correlation width is very broad (short focal length and tight pump focusing), then each single mode spreads across many pixels and overlaps with the other modes. In both cases, the HOM interference visibility is lost. Instead, the highest HOM interference visibility is obtained when each pixel acts as a single-mode detector, that is, when the correla-

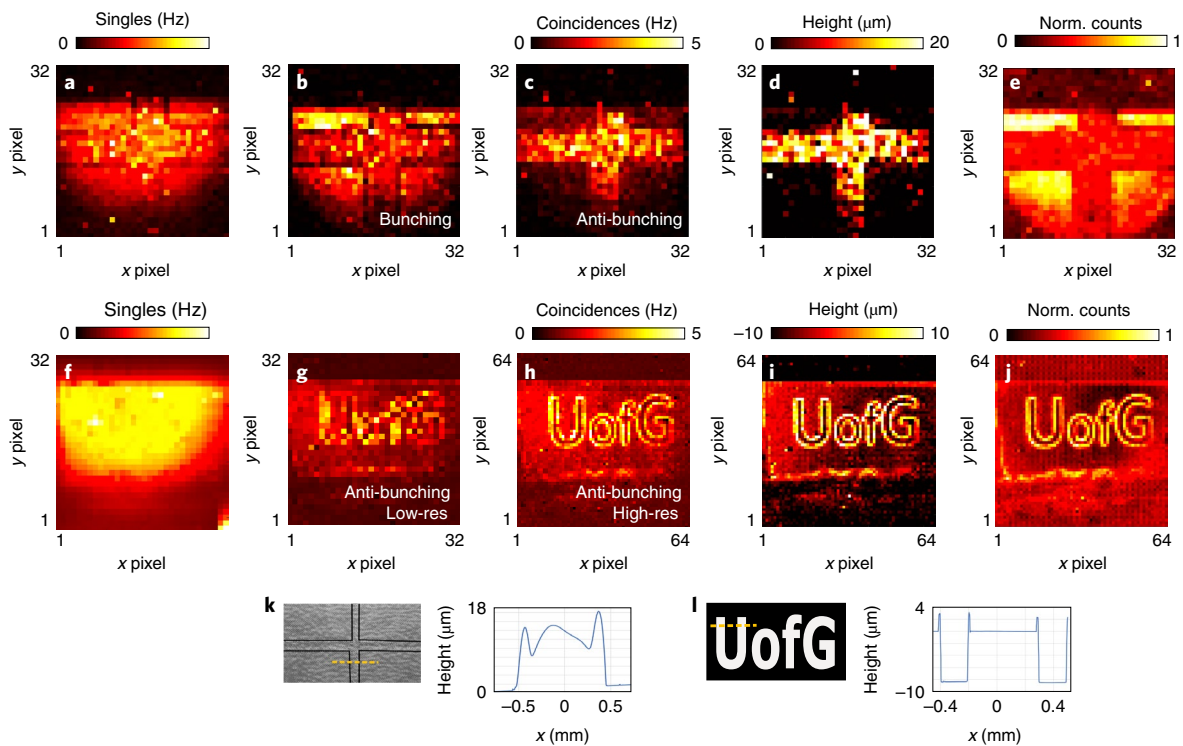


Fig. 5 | Full-field HOM imaging. **a**, Intensity image captured by the SPAD camera of a clear acrylic cross pattern on a microscope slide. **b,c**, Bunching (from adjacent pixels) (**b**) and anti-bunching (**c**) coincidence maps. **k**, Image of the sample and profile measurement taken along the yellow dashed line; the average height is $12.9 \mu\text{m}$. **d**, Number of coincidence events is converted to a height measurement relative to the surface of the microscope slide. **e**, Combination of weighted bunching and anti-bunching images produces a normalized image with reduced noise. **f**, Intensity image of the letters ‘UofG’ etched to a depth of $8.36 \mu\text{m}$ into a glass substrate. **g,h**, Anti-bunching (from adjacent pixels) at the native camera resolution of 32×32 pixels (**g**) and 64×64 pixels super-resolved image obtained by the 2×2 raster-scanning camera (**h**). **i**, Image of the sample and profile measurement taken along the yellow dashed line. **j**, Depth map of the sample obtained from the coincidence map in **h**. **j**, Combination of weighted bunching and anti-bunching images produces a normalized image with reduced noise. The pixel pitch is $150 \mu\text{m}$.

tion width is of the same order of the camera pixel size of $150 \mu\text{m}$ (in our case, this corresponds to $f_0 = 300 \text{ mm}$). The insets in Fig. 3d show the measured biphoton distributions. The dashed curve shows a model for the HOM dip visibility for our experiment with no free parameters and confirms the role and importance of tailoring the spatial mode content of the quantum light field on the camera.

Full-field HOM interferometry. Figure 4 shows the spatially resolved bunching and anti-bunching coincidence maps for five different delays over one-half of the sensor, the other half simply being a symmetric image containing the same information. As the spatial delay of the interferometer tends to zero, the number of bunching events increases to the maximum, whereas the anti-bunching events tend to zero. Crucial to our HOM imaging technique, this full-field HOM measurement shows the direct pixel-wise-resolved mapping between the spatial delay and number of coincidence events.

HOM imaging. The first sample was prepared by spraying a layer of clear acrylic on a glass substrate, forming a cross pattern with a depth of $12.9 \mu\text{m}$, averaged along the dashed line (Fig. 5k), as measured with a profilometer. Figure 5a shows the intensity (photon counts) image recorded by the SPAD camera. The sample itself, as expected, is not visible, although the edges are barely visible probably due to scattering that leads to an effective loss. The HOM images are extracted from the JPD data reconstructed from a total of 130 million intensity frames (total acquisition time, 37 min) (Fig. 5b,c shows the bunching and anti-bunching coincidence events, respectively). These images show a clear contrast between

the acrylic surface and its surroundings with the anti-bunching and bunching images that appear as reverse-contrast images of each other due to the conservation of probability (that is, with small discrepancies due to noise and any losses).

We use the spatially resolved coincidence counts versus delay in $4 \mu\text{m}$ steps (five delays are shown in Fig. 4) as a depth estimator and obtain the relative depth profile (Fig. 5c) of the sample shown in Fig. 5d. From this, we estimate the average thickness of the layer of acrylic to be $14.5 \pm 6.0 \mu\text{m}$, in relatively good agreement with the ground-truth measured value. We note the large error (standard deviation) around the average value, which is due to the fact that the sample itself is not uniform but also due to the obvious noise in the images. However, a recent work showed that photon-number-resolving information can increase the precision in (lossy) conventional HOM sensing by combining bunching and anti-bunching signals⁷ (Methods). A substantially improved image is then retrieved (Fig. 5e), which has a variance that is 3.4 times smaller compared with the direct measurement (Fig. 5c) in the cross region of the image.

A second sample was fabricated by etching the letters ‘UofG’ onto a glass substrate to a depth of $8.36 \mu\text{m}$ (measured with a profilometer; Fig. 5k shows the profile along the yellow dashed line) and width of the lettering etch ($230 \mu\text{m}$). Figure 5f shows the intensity image that does not reveal any details about the shape of the etched sample. Figure 5g shows the anti-bunching coincidence image at the camera’s native resolution of 32×32 pixels. The ‘UofG’ pattern is visible, but is strongly under-resolved. We, therefore, also performed a 2×2 raster scan to increase the pixel resolution by a factor of four

(by simple ‘shift and add’ of the four raster-scanned images³⁴): the sample is now clearly visible in the anti-bunching HOM image (Fig. 5h). We note that the cross/UofG patterns have positive/negative thickness step changes with respect to the substrate: our technique does not require prior knowledge of this; rather, changes in the coincidence counts are positive/negative, directly indicating whether the features on the substrate are positive or negative variations in thickness. We also observe high counts at the edges of the etched regions. This is due to the very sharp profile of etching (compared with the relatively smooth edges of the acrylic sample) that leads to edge diffraction along the contours of the letters. This diffraction introduces additional transverse wavevector components on the transmitted photons, which reduces indistinguishability between the signal and idler photons and a higher coincidence rate with respect to the surrounding non-etched parts. Figure 5i shows the retrieved depth image from the high-resolution coincidence image from which we estimate an etching depth of $8.2 \pm 1.2 \mu\text{m}$, in very good agreement with the ground-truth reference measurement, as well as shows a relatively low error that is in line with typical HOM measurements that use single-point detection. As for the case of the cross, a weighted combination of the bunching and anti-bunching data has reduced noise with reduced variance of 1.6 times inside the letters (Fig. 5j).

Conclusions. HOM interference can be used in full-field imaging to directly retrieve spatially resolved depth profiles of transparent samples. Access to both bunching and anti-bunching images can be used to also assess losses and, in turn, reduce the noise variance in the images by up to nearly an order of magnitude in the best-case scenario.

To put these measurements into context, we note that the average coincidence values are of the order of 1 Hz for each pixel, which at 60,000 frames per second implies roughly only one frame in every 60 frames detecting an actual photon pair. If we consider the photon detection probability of the camera (80% fill factor and 6% quantum efficiency), this corresponds to an actual average photon-pair flux in the interferometer of ~ 400 photon pairs per second at each pixel or ~ 7 photon pairs per frame. This is extremely low, yet it allows us to retrieve clear images with micrometre-level absolute precision in the depth measurements. Photon density and total illumination on the sample are also often quoted as a concern for some bio-imaging applications. The results shown here were performed in a regime in which $\sim 10^5$ photons at each pixel are required to illuminate the sample for the total minimum exposure time of ~ 20 min (if the camera is operated at 96,000 frames per second). This can possibly be further reduced by more than an order of magnitude by improving the camera technology; indeed, photon-pair detection scales quadratically with the quantum efficiency of the camera. HOM imaging, therefore, provides an opportunity, for example, for label-free bio-imaging or the imaging of photoinduced effects that may require very low photon fluxes. Then, the illumination source itself does not modify the biological sample or at least provides controlled modification at the level of single photons³⁵.

New-generation asynchronous read-out SPAD cameras that can operate at ~ 50 MHz rates^{36,37} and have already been used to nearly increase up to the video frame rate of other challenging imaging feats such as non-line-of-sight imaging³⁸ would also provide a 1,000-fold decrease in acquisition times, potentially leading to video-frame-rate imaging capability. An increase in count rates would also allow to apply high-precision HOM sensing approaches with 10–100 nm sensitivity and competing with classical interferometric approaches, although with advantages of better stability and better axial field of view that extends over tens of micrometres rather than a few hundred nanometres.

The methods demonstrated here can also be transferred, for example, to quantum optical coherence tomography that essentially

also leverages photon bunching to detect multiple interfaces and layered structures.

Online content

Any methods, additional references, Nature Research reporting summaries, source data, extended data, supplementary information, acknowledgements, peer review information; details of author contributions and competing interests; and statements of data and code availability are available at <https://doi.org/10.1038/s41566-022-00980-6>.

Received: 4 July 2021; Accepted: 18 February 2022;

Published online: 11 April 2022

References

- Hong, C. K., Ou, Z. Y. & Mandel, L. Measurement of subpicosecond time intervals between two photons by interference. *Phys. Rev. Lett.* **59**, 2044–2046 (1987).
- Lee, S.-Y. & Nha, H. Second-order superposition operations via Hong-Ou-Mandel interference. *Phys. Rev. A* **85**, 043816 (2012).
- Zhang, Y. et al. Engineering two-photon high-dimensional states through quantum interference. *Sci. Adv.* **2**, e1501165 (2016).
- Kok, P. et al. Linear optical quantum computing with photonic qubits. *Rev. Mod. Phys.* **79**, 135–174 (2007).
- Nagali, E. et al. Optimal quantum cloning of orbital angular momentum photon qubits through Hong-Ou-Mandel coalescence. *Nat. Photon.* **3**, 720–723 (2009).
- Lyons, A. et al. Attosecond-resolution Hong-Ou-Mandel interferometry. *Sci. Adv.* **4**, eaap9416 (2018).
- Scott, H., Branford, D., Westerberg, N., Leach, J. & Gauger, E. M. Beyond coincidence in Hong-Ou-Mandel interferometry. *Phys. Rev. A* **102**, 33714 (2020).
- Bornman, N. et al. Ghost imaging using entanglement-swapped photons. *npj Quantum Inf.* **5**, 63 (2019).
- Bornman, N., Prabhakar, S., Vallés, A., Leach, J. & Forbes, A. Ghost imaging with engineered quantum states by Hong-Ou-Mandel interference. *New J. Phys.* **21**, 073044 (2019).
- Genovese, M. Real applications of quantum imaging. *J. Opt.* **18**, 073002 (2016).
- Moreau, P.-A., Toninelli, E., Gregory, T. & Padgett, M. J. Imaging with quantum states of light. *Nat. Rev. Phys.* **1**, 367–380 (2019).
- Gilaberte Basset, M. et al. Perspectives for applications of quantum imaging. *Laser Photonics Rev.* **13**, 1900097 (2019).
- Moreau, P.-A., Mougin-Sisini, J., Devaux, F. & Lantz, E. Realization of the purely spatial Einstein-Podolsky-Rosen paradox in full-field images of spontaneous parametric down-conversion. *Phys. Rev. A* **86**, 010101 (2012).
- Edgar, M. et al. Imaging high-dimensional spatial entanglement with a camera. *Nat. Commun.* **3**, 984 (2012).
- Lubin, G. et al. Quantum correlation measurement with single photon avalanche diode arrays. *Opt. Express* **27**, 32863–32882 (2019).
- Ianzano, C. et al. Fast camera spatial characterization of photonic polarization entanglement. *Sci. Rep.* **10**, 6181 (2020).
- Ndagano, B. et al. Imaging and certifying high-dimensional entanglement with a single-photon avalanche diode camera. *npj Quantum Inf.* **6**, 94 (2020).
- Morris, P. A., Aspdén, R. S., Bell, J. E. C., Boyd, R. W. & Padgett, M. J. Imaging with a small number of photons. *Nat. Commun.* **6**, 5913 (2015).
- Moreau, P.-A., Toninelli, E., Gregory, T. & Padgett, M. J. Ghost imaging using optical correlations. *Laser Photonics Rev.* **12**, 1700143 (2018).
- Devaux, F., Mosset, A., Bassignot, F. & Lantz, E. Quantum holography with biphotons of high Schmidt number. *Phys. Rev. A* **99**, 033854 (2019).
- Lemos, G. B. et al. Quantum imaging with undetected photons. *Nature* **512**, 409–412 (2014).
- Defienne, H., Reichert, M., Fleischer, J. W. & Faccio, D. Quantum image distillation. *Sci. Adv.* **5**, eaax0307 (2019).
- Gregory, T., Moreau, P.-A., Toninelli, E. & Padgett, M. J. Imaging through noise with quantum illumination. *Sci. Adv.* **6**, eaay2652 (2020).
- Camphausen, R. et al. A quantum-enhanced wide-field phase imager. *Science Advances* **7**, eabj2155 (2021).
- Defienne, H. et al. Pixel super-resolution using spatially-entangled photon pairs. Preprint at <https://arxiv.org/abs/2105.10351> (2021).
- Defienne, H., Ndagano, B., Lyons, A. & Faccio, D. Polarization entanglement-enabled quantum holography. *Nat. Phys.* **17**, 591–597 (2021).
- Morimoto, K. et al. Megapixel time-gated SPAD image sensor for 2D and 3D imaging applications. *Optica* **7**, 346–354 (2020).
- Morimoto, K. & Charbon, E. High fill-factor miniaturized SPAD arrays with a guard-ring-sharing technique. *Opt. Express* **28**, 13068–13080 (2020).

29. Radoslaw, C., Jachura, M., Banaszek, K. & Wasilewski, W. Hologram of a single photon. *Nat. Photon.* **10**, 576–579 (2016).
30. Ibarra-Borja, Z., Sevilla-Gutiérrez, C., Ramírez-Alarcón, R., Cruz-Ramírez, H. & U'Ren, A. B. Experimental demonstration of full-field quantum optical coherence tomography. *Photon. Res.* **8**, 51–56 (2020).
31. Devaux, F., Mosset, A., Moreau, P.-A. & Lantz, E. Imaging spatiotemporal Hong-Ou-Mandel interference of biphoton states of extremely high Schmidt number. *Phys. Rev. X* **10**, 031031 (2020).
32. Restuccia, S. et al. Photon bunching in a rotating reference frame. *Phys. Rev. Lett.* **123**, 110401 (2019).
33. Defienne, H., Reichert, M. & Fleischer, J. W. General model of photon-pair detection with an image sensor. *Phys. Rev. Lett.* **120**, 203604 (2018).
34. Farsiu, S., Robinson, M., Elad, M. & Milanfar, P. Fast and robust multiframe super resolution. *IEEE Trans. Image Process.* **13**, 1327–1344 (2004).
35. Phan, N. M., Cheng, M. F., Bessarab, D. A. & Krivitsky, L. A. Interaction of fixed number of photons with retinal rod cells. *Phys. Rev. Lett.* **112**, 213601 (2014).
36. Renna, M. et al. Fast-gated 16×1 SPAD array for non-line-of-sight imaging applications. *Instruments* **4**, 14 (2020).
37. Riccardo, S., Conca, E., Sesta, V. & Tosi, A. Fast-gated 16×16 SPAD array with on-chip 6 ps TDCs for non-line-of-sight imaging. In *2021 IEEE Photonics Conference (IPC)* 1–2 (IEEE, 2021).
38. Nam, J. H. et al. Low-latency time-of-flight non-line-of-sight imaging at 5 frames per second. *Nat. Commun.* **12**, 6526 (2021).

Publisher's note Springer Nature remains neutral with regard to jurisdictional claims in published maps and institutional affiliations.

© The Author(s), under exclusive licence to Springer Nature Limited 2022

Methods

Experimental layout. Signal–idler photon pairs are generated via a type-I SPDC in a 0.5-mm-long β -barium borate (BBO) crystal. The generated photons are spatially separated in the far field of the BBO crystal using a D-shaped mirror. The signal photon travels through a delay line where the path length can be adjusted using a motorized translation stage. The idler photon travels through a fixed-length path where a dove prism performs image inversion in the transverse plane. Both signal and idler photons propagate through identical 4f imaging systems that relay the far field of the BBO crystal (image plane of the D-shaped mirror) to planes P_1 and P_2 ; the sample to be imaged is subsequently placed in the latter plane. The image of planes P_1 and P_2 are overlapped using a 50:50 BS and imaged using identical imaging systems in both output ports, onto an SPAD camera (SPC³, MPD) with an array of 32×64 pixels, $\sim 78\%$ fill factor and $150 \mu\text{m}$ pixel pitch. The camera has a quantum efficiency of $\sim 9\%$ at the photon-pair wavelength (694 nm), nominal frame rate of 96,000 frames per second and a dark count rate of 0.14 counts per pixel per second. For most of the experiments, the camera was operated at 60,000 frames per second due to software/computer limitations.

Choice of pump laser. The camera is internally triggered, implying that a continuous-wave laser can also be used for SPDC generation, ideally with as short a wavelength as possible to benefit from the higher quantum efficiency of the camera at shorter SPDC wavelengths (for example, $\sim 10\%$ at 700 nm compared with $\sim 4\%$ at 800 nm). However, the choice of a pulsed laser source also provides photons with a broader bandwidth, that is, a narrower HOM interference dip and consequently larger variations in the coincidence counts for a given sample thickness.

Lateral spatial resolution. The lateral spatial resolution is set by the biphoton correlation width. As shown in Fig. 3, this needs to be matched to the pixel size for optimum HOM visibility; then, the field of view and lateral spatial resolution are set by the camera in a lens-less configuration. In our measurements, this gives a field of view (determined by the camera chip size) of $4.8 \times 4.8 \text{ mm}^2$ with 0.15 mm resolution (improved to 0.75 mm by raster scanning). One can alternatively focus the correlation width to a diffraction-limited spot onto a sample to increase the resolution and then magnify the SPDC to mode match the pixel size onto the SPAD. The field of view would then be $4.8 \times 4.8/M^2 \text{ mm}^2$, where M is the magnification factor of the system; the resolution now becomes the width of the diffraction-limited spot.

JPD measurements. At each delay position, we reconstructed the JPD data from a total of 19 million intensity frames and measured the HOM dip with a visibility of $88 \pm 2\%$. Then, to estimate the number of bunching events, we used two approaches. The first consists of fitting a Gaussian peak to the minus-coordinate projection and use the peak as the estimate. Using this approach, we measured the HOM peak visibility of $81 \pm 7\%$, comparable to that obtained for the HOM dip. The second approach exploits the fact that (1) the two-photon correlation width is larger than one pixel and (2) the SPAD camera has a relatively high fill factor (80%). Thus, we can estimate the number of bunching events where photons are incident on adjacent pixels, that is, the coincidences are generated from the conditional distribution $\Gamma(\mathbf{r}|\mathbf{r} + \Delta\mathbf{r})$, where $\Delta\mathbf{r}$ is a transverse shift by a single pixel and averaged over the four nearest-neighbour pixels. The visibility measured in this case is $60 \pm 7\%$. This lower value is to be expected given that adjacent pixels capture different spatial modes, thus increasing photon distinguishability.

Dependence of HOM dip visibility on biphoton correlation width. The biphoton correlation width scales linearly with the pump laser-beam area, which, in turn, scales quadratically with f_0 . This is used (Fig. 3d) to estimate the biphoton correlation width and thus map f_0 (upper horizontal axis) to R (lower horizontal axis) for all f_0 , starting from the measurement at $f_0 = 300 \text{ mm}$ that gives a biphoton correlation width equal to the camera pixel width ($R = 1$); all other R values are consequently scaled quadratically with f_0 .

Predicting the HOM dip visibility as a function of R . The biphoton correlation function can be expanded in terms of the Hermite–Gauss modes. We limit our one-dimensional toy model to an equal superposition of the fundamental and first-order modes, as this captures both cases of spatially symmetric and anti-symmetric states leading to bunching and anti-bunching, respectively³⁹. A calculation (similar to another study³⁹) then yields the coincidence probability between positions x_1 and x_2 on the two halves of the detector at delay δ of

$$P_C(x_1, x_2, \delta) = \psi_+^2(x_1, x_2) + \psi_-^2(x_1, x_2) + 2\psi_+(x_1, x_2)\psi_-(x_1, x_2)\exp[-\delta^2/(2\Sigma^2)],$$

where Σ is the HOM dip width and

$$\psi_{\pm}(x_1, x_2) = \pm \mathcal{N} e^{-(x_1+x_2)^2/2\sigma_{\text{corr}}^2} e^{-\beta^2(x_1-x_2)^2/w^2} \left[1 \pm \frac{\sqrt{2}}{\sigma_{\text{corr}}}(x_1+x_2) \right].$$

Here $\sigma_{\text{corr}} = \sqrt{L_c/\beta^2 k_p}$ is the correlation width; k_p and w are the pump wavenumber and width, respectively; L_c is the crystal length; \mathcal{N} is a normalization

constant; and β is a scaling constant to account for diffraction during propagation between the crystal and detector. Keeping the illumination area (w/β) constant for different pump-beam sizes (w) leads to an effective change in the correlation length ($\sigma_{\text{corr}} = \sqrt{L_c/\beta^2 k_p}$); for instance, $\beta^{-1} \simeq \{50, 25, 15\}$ for focal lengths $f_0 = \{150, 300, 500\} \text{ mm}$. The probability of detection at the i th and j th pixels on each detector half is given by the integral over the pixel area. We, thus, introduce pixels of size ΔL and with effective loss rate $\gamma = 1 - (\text{fill factor}) \times (\text{quantum efficiency})$ and integrate $P_C(x_1, x_2, \delta)$ over the interval $L_i = [-L/2 + (i + \gamma/2)\Delta L, -L/2 + (i + 1 - \gamma/2)\Delta L]$ for x_1 and L_j over the same range for x_2 , where L is the total width of the (half)-array; $P_C^i(\delta) = \int_{L_i} dx_1 \int_{L_j} dx_2 P_C(x_1, x_2, \delta)$ is the coincidence probability between pixel i and pixel j . The total coincidence probability is finally given by $P_C(\delta) = \sum_{ij} P_C^i(\delta)$. We compute the visibility as

$$V = \frac{P_C(\delta \rightarrow \infty) - P_C(\delta = 0)}{P_C(\delta \rightarrow \infty) + P_C(\delta = 0)}, \quad (2)$$

which yields the plot (Fig. 3d, dashed curve) that captures the overall trend with $R = \Delta L/(2\sqrt{2\ln 2}\sigma_{\text{corr}})$ and the following experimentally relevant parameters are used: $\gamma = 1 - 0.09 \times 0.78 = 0.93$, $k_p = 2\pi/347 \text{ nm}$, $L_c = 0.5 \text{ mm}$.

Photon-number resolution approach for improved signal-to-noise ratio. We can provide an estimate of the noise in each image by analysing the count statistics across pixels that are uniformly illuminated. For example, Fig. 5f shows a region of about 200 pixels that is illuminated by the central and uniform region of parametric downconversion emission. Across these pixels, we evaluate the ratio of the standard deviation of the square root of the mean count value to be 1.26, that is, the camera pixels report counts that are ~ 1.3 times the shot-noise limit.

Noise in these measurements has several origins: losses in the system, dark count noise on the camera, pixel fill factor and effective photon loss on the camera due to the 5–10% quantum efficiency. These losses then quadratically affect the photon coincidence images, that is, the noise in photon-pair counting is given by the product of the noise of the two individual photons.

In the presence of photon loss (or detectors with limited efficiency), distinguishing single-photon clicks from bunching and coincidence events can increase the precision of HOM-based sensing⁷. The HOM signal is not constrained to the anti-diagonal ($k_x = -k_x$) of the JPD, which indicates coincidence between a pixel and its coincidence partner; additional coincidence and bunching information is found through the JPD terms correlating a pixel with the neighbours of itself and of its coincidence partner (the non-zero values of the sum and minus coordinates are shown in Fig. 3) that arise due to a correlation-based point spread function, which—although matched to the pixel size (as described in the main text)—spreads across the adjacent pixels due to its Gaussian-like distribution. These latter terms allow us to harness the number-resolving advantage in the fundamental HOM experiment⁷ as well as addressing array-specific noise contributions³⁶. To account for different quality dips across the images, we rescale the images based on image regions of constant coincidence counts. For example, with a mask, we select the inner or outer regions of the cross and the inner or outer regions of ‘UofG’ lettering. These rescaled images are then combined according to the estimator for a common signal in multiple independent noisy channels— $\hat{\theta} = [\sum_j \sigma_j] \sum_j (x_j/\sigma_j)$ —to obtain a minimum-variance estimate⁴⁰. Here j denotes the anti-bunching and bunching images that are, therefore, summed together with relative weights given by the σ_j values, namely, the associated standard deviation in the counts used as a noise estimate and are computed in an image region of constant coincidence counts.

Data availability

The experimental data that support the findings presented here are available from <https://doi.org/10.5525/gla.researchdata.1241>.

Code availability

The codes that support the findings presented here are available from <https://doi.org/10.5525/gla.researchdata.1241>.

References

- Walborn, S. P., de Oliveira, A. N., Pádua, S. & Monken, C. H. Multimode Hong–Ou–Mandel interference. *Phys. Rev. Lett.* **90**, 143601 (2003).
- Kay, S. M. *Fundamentals of Statistical Signal Processing: Estimation Theory* (Prentice–Hall, 1993).

Acknowledgements

We thank M. Cromb for fruitful discussions on the interpretation of the results. We acknowledge financial support from the UK Engineering and Physical Sciences Research Council (grants EP/R030413/1, EP/M01326X/1 and EP/R030081/1) and from the European Union’s Horizon 2020 research and innovation programme under grant agreement no. 801060. D.F. acknowledges support from the Royal Academy of Engineering Chair in Emerging Technologies programme. H.D. acknowledges support

from the European Union's Horizon 2020 research and innovation programme under the Marie Skłodowska-Curie grant agreement no. 840958. N.W. acknowledges support from the Royal Commission for the Exhibition of 1851.

Author contributions

D.F. conceived the concept and supervised the work. B.N., H.D., A.L. and D.F. conceived and discussed the experimental setup. B.N. performed the experiment. Y.D.S. microfabricated the etched sample. D.B., N.W. and E.M.G. applied noise reduction approaches. All the authors contributed to the analysis of the results and the manuscript.

Competing interests

The authors declare no competing interests.

Additional information

Correspondence and requests for materials should be addressed to Daniele Faccio.

Peer review information *Nature Photonics* thanks the anonymous reviewers for their contribution to the peer review of this work.

Reprints and permissions information is available at www.nature.com/reprints.